



Delft University of Technology

Confirming Debonding of Non-Metallic Inclusions as an Important Factor in Damage Initiation in Bearing Steel

Nikolic, Ksenija; De Wispelaere, Jelle; Ravi, Gopalakrishnan; Hertelé, Stijn; Depover, Tom; Verbeken, Kim; Petrov, Roumen H.

DOI

[10.3390/met13061113](https://doi.org/10.3390/met13061113)

Publication date

2023

Document Version

Final published version

Published in

Metals

Citation (APA)

Nikolic, K., De Wispelaere, J., Ravi, G., Hertelé, S., Depover, T., Verbeken, K., & Petrov, R. H. (2023). Confirming Debonding of Non-Metallic Inclusions as an Important Factor in Damage Initiation in Bearing Steel. *Metals*, 13(6), Article 1113. <https://doi.org/10.3390/met13061113>

Important note

To cite this publication, please use the final published version (if applicable).
Please check the document version above.

Copyright






Other than for strictly personal use, it is not permitted to download, forward or distribute the text or part of it, without the consent of the author(s) and/or copyright holder(s), unless the work is under an open content license such as Creative Commons.

Takedown policy

Please contact us and provide details if you believe this document breaches copyrights.
We will remove access to the work immediately and investigate your claim.

Article

Confirming Debonding of Non-Metallic Inclusions as an Important Factor in Damage Initiation in Bearing Steel

Ksenija Nikolic ^{1,2,*} , Jelle De Wispelaere ¹, Gopalakrishnan Ravi ¹, Stijn Hertelé ¹ , Tom Depover ³ , Kim Verbeken ³  and Roumen H. Petrov ^{1,4} 

¹ Department Electromechanical, Systems & Metal Engineering, Ghent University, Technologiepark 46, 9052 Ghent, Belgium; stijn.hertele@ugent.be (S.H.); roumen.petrov@ugent.be (R.H.P.)

² SIM VZW, Technologiepark 48, 9052 Ghent, Belgium

³ Department Materials, Textiles and Chemical Engineering, Ghent University, Technologiepark 46, 9052 Ghent, Belgium; tom.depover@ugent.be (T.D.); kim.verbeken@ugent.be (K.V.)

⁴ Department of Materials Science and Engineering, Delft University of Technology, Mekelweg 2, Delft 2600, The Netherlands

* Correspondence: ksenija.nikolic@ugent.be

Abstract: Damage in bearings is closely associated with the presence of microstructural alterations, known as white etching areas (WEAs) and white etching cracks (WECs). One of the main reasons for the creation of these microstructural alterations is the presence of defects in the material, such as non-metallic inclusions. Manganese sulfides and aluminum oxides are widely reported in the literature as the most common types of non-metallic inclusions found in bearing steels. This study classifies 280 non-metallic inclusions in an investigated bearing steel according to several criteria: bonded/debonded with the matrix, size, shape, orientation angle, depth below the raceway surface, and chemical composition. Contrary to the findings in the literature, this investigation reports that the chemical composition of the inclusion ($\text{MnS} + \text{Al}_2\text{O}_3$) is of secondary importance when considering factors for damage initiation. The orientation of the microstructural alterations is observed to coincide with the high-stress regions, indicating a relation between the formation of butterfly wings and the white etching crack. In our investigation, butterfly wings typically exhibit a 45-degree pattern originating from the non-metallic inclusions. Conversely, the white etching crack starts from the non-metallic inclusion at a shallower angle in correspondence to the raceway. This can be attributed to the stress state, which corresponds to a region where extensive white etching cracks are formed. In conclusion, the microstructural observations demonstrate that the state of non-metallic inclusion—i.e., whether they are bonded or not to the steel matrix—plays an essential role in initiating rolling contact fatigue damage.

Keywords: bearing steel; white etching cracks; white etching area; non-metallic inclusions; damage; rolling contact fatigue



Citation: Nikolic, K.; De Wispelaere, J.; Ravi, G.; Hertelé, S.; Depover, T.; Verbeken, K.; Petrov, R.H.

Confirming Debonding of Non-Metallic Inclusions as an Important Factor in Damage Initiation in Bearing Steel. *Metals* **2023**, *13*, 1113. <https://doi.org/10.3390/met13061113>

Academic Editor: Chenguang Bai

Received: 23 May 2023

Revised: 2 June 2023

Accepted: 10 June 2023

Published: 13 June 2023



Copyright: © 2023 by the authors. Licensee MDPI, Basel, Switzerland. This article is an open access article distributed under the terms and conditions of the Creative Commons Attribution (CC BY) license (<https://creativecommons.org/licenses/by/4.0/>).

1. Introduction

Wind energy is an important sector for achieving the carbon neutrality target in the European energy system and is the fastest-growing renewable energy source globally. The European Union established a new renewable energy target of at least 32% by 2030 [1]. Global offshore wind installations are increasing in number, and turbine sizes continue to grow. However, the wind industry still faces the problem of premature failure of components, which affects the cost of operation and maintenance [2,3]. The failure rate of electrical and electronic control systems is higher than that of the drivetrain and gearbox. However, replacing the gearbox is more expensive due to its size, which increases cost and downtime. According to a database published in 2016, bearings account for the majority (76%) of wind turbine gearbox failures [4].

Bearing failures occur within less than 20% of the calculated L_{10} lifetime [5] due to the process involving white etching cracks (WECs). Most of the failures associated with white etching cracks can be explained by surface or subsurface initiation. Surface-induced damage points to the decomposition of lubrication [6–10], electrical current [9,11–13], and hydrogen diffusion into bulk material [14–17]. Under favorable lubrication conditions (low friction coefficient, no decomposition of the oil that may cause H ingress, etc.), the stresses and resulting damage in a bearing primarily occur within the subsurface region of the bulk material [18]. The magnitude of subsurface stress is directly related to the maximum contact pressure. The specific depth at which the highest stress occurs can be accurately determined using Hertz theory [19], taking into account the contact geometry. The subsurface mechanism suggests non-metallic inclusions [20–30], defects such as voids [31,32], and large carbides [33] as the points of damage initiation. The altered microstructure, also known as the white etching area (WEA), consists of nanocrystalline ferrite with a grain size in the range of 10–300 nm [32,34–36]. Atom probe tomography detected carbon segregation at the grain boundaries, suggesting that carbon plays a vital role in extreme grain refinement [37,38]. This zone is reported to be 30–50% harder than the martensitic matrix [39,40].

Non-metallic inclusions in steel result from the steel-making process and can be classified considering the moment at which they form with respect to the solidification process: primary (before solidification) and secondary (after solidification) [41]. The most common non-metallic inclusions in bearing steels are MnS, Al_2O_3 , Ti(C, N), and Ca aluminates [42]. Due to their different thermal expansion coefficients from the matrix, they can develop tensile and compressive residual stresses during cooling to ambient temperature. Even though advancements have been made in producing cleaner steel [43], their presence in bearing steel is thought to remain primarily responsible for the formation of white etching cracks.

It is reported that WECs can form from butterfly wings (BW), although not exclusively [23]. The term butterfly wings is derived from their two-dimensional appearance. The BWs form around non-metallic inclusions with two distinct boundaries. Typically, one boundary contains a crack propagating from the non-metallic inclusion while the other is crack-free [44]. Evans et al. [26] performed serial sectioning of an industrial planet bearing and transient test bearing. A high likelihood of inclusions initiating WECs was reported, mostly associated with MnS. The average lengths of the inclusions that interacted with the WEC were less than 10 and 20 μm for the planet and transient test bearing, respectively, suggesting that the inclusion's density should be taken into account in addition to the inclusion's length to understand the formation of the WEC/WEA. Furthermore, evidence of BWs extending into a WEC was found. In a different study, the same authors successfully reproduced WECs from the test rig under low maximum contact pressure (1200 MPa) [24]. Serial sectioning revealed that most WECs did not reach the contact surface, confirming the subsurface initiation mechanism. Different types of non-metallic inclusions, relatively small in size (~2–15 μm), interacted with WECs. Gould et al. [20] studied a spherical roller bearing used in an industrial application by tomographic analysis. The cracks investigated in this study were small enough to be contained within the sample volume, aiming to understand the initiation point of WEC phenomena. The findings showed that all four cracks started from large non-metallic inclusions and were elongated in the over-rolling direction. In addition, all four inclusions contained a combination of aluminum, manganese, and sulfur. The findings indicated the potentially harmful nature of so-called multi-phase inclusions. Crack morphology was reported to be the same in all cases with the “upside-down U”. The authors suggested that the repeatability of the crack morphology points to the stress state that deviates these cracks in a certain direction. Bruce et al. [20] catalogued inclusions from the failed planet bearing. Four distinct forms of damage were reported: internal cracking, crack propagation into the bulk material without an attached WEA, separation from the surrounding material, and WEC initiation. Neither internal cracking nor inclusion separation was observed from the bulk material for a distance greater than 420 μm below

the raceway surface, although WECs were present at 630 μm . Smaller inclusions (8–16 μm) tended to initiate longer WECs.

Recent work on the bonding of non-metallic inclusions with the steel matrix and their relationship to damage is a growing area of interest [21,28,45]. Al-Tameemi [21] employed atomic force microscopy to show the separation of MnS inclusion from the steel matrix, suggesting the occurrence of shear or tensile stresses in this region. Furthermore, the length of inclusions was directly proportional to the length of butterflies. Vegter et al. [28] applied tensile testing in combination with digital image correlation on bearing steel. Coarser Al_2O_3 inclusions were found to be debonded from the bulk material and, as such, a crack initiation point during rolling contact fatigue. However, most studies reported the debonding of the non-metallic inclusions as a form of damage during rolling contact fatigue, and the initial state of (de)bonding was not characterized.

This work aims to contribute to the understanding of the effect of bonding between the matrix and inclusions on subsurface damage initiation in field-loaded bearings. To reach this goal, the non-metallic inclusions in a field-loaded bearing were characterized and correlated to their size, distance from the raceway surface, orientation, chemical composition, and shape. Furthermore, the link with damage development in relation to the distance below the raceway surface was established.

2. Experimental Procedure

2.1. Material and Sample Preparation

In this work, we investigated a failed tapered roller bearing that operated in a wind turbine. The bearing was removed from the gearbox following the formation of an axial crack. All specimens were extracted from the inner ring. The specimens are made of AISI 52100 martensitic steel and have a chemical composition as shown in Table 1. The resulting microstructure consists of tempered martensite, spheroidal carbides homogeneously distributed in the martensitic matrix, and transition carbides [42]. Transition carbides are precipitates formed during tempering treatment from supersaturated martensite; they include η and ϵ carbides [46]. To examine the presence of non-metallic inclusions (NMIs) and any associated damage in the bearing, 4 samples were cut from the zone of interest along circumferential and axial planes in the loaded zone (Figure 1). Samples were prepared for metallographic observation using a Struers (Struers, Ballerup, Denmark) type 50A15 cut-off wheel on a Discotom-5 cutting machine. Cutting was performed at a low speed and with underwater cooling to prevent any heating of the sample that may cause phase transformation or other microstructural changes. Next, the samples were embedded in a conductive polymer and ground with SiC grinding papers, followed by polishing with diamond paste. The final polishing step used colloidal silica (OPS) with a particle size of 35 nm. The microstructure of the samples was characterized for the presence of damage by etching with 2% Nital (2% vol% HNO_3 solution in $\text{C}_2\text{H}_5\text{OH}$). Scanning electron microscopy (SEM) images were acquired using an FEI Quanta 450-FEG-SEM (ThermoFisher, Hillsboro, OR, USA) operating at 15 kV, with a final beam aperture of 50 μm , and a spot size #5 corresponding to a probe current of 2.3 nA. All samples were observed in secondary electron (SE) and backscattered electron (BSE) imaging modes. The chemical composition of the inclusions was determined using energy-dispersive X-ray spectroscopy (EDS) on the EDAX TEAMTM EDS system (EDAX AMETEK BV, Tilburg, The Netherlands).

Table 1. Chemical composition of the investigated bearing.

Element	C	Mn	P	S	Si	Cr	Cu	Mo	Ni	Fe
Wt. %	0.96	0.27	0.02	0.01	0.25	1.6	0.2	0.15	0.18	Bal.

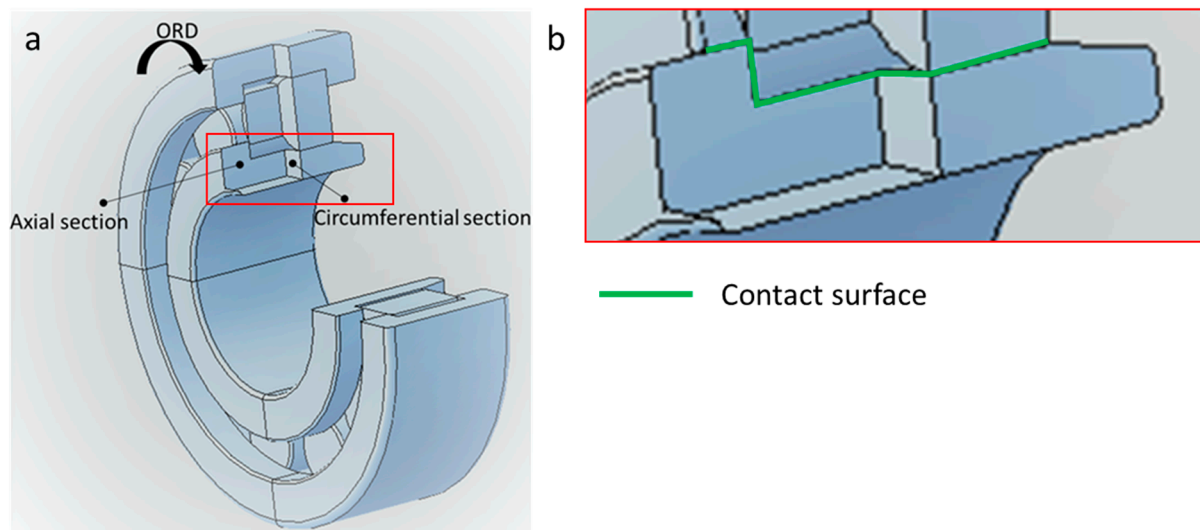


Figure 1. (a) Schematic drawing of the bearing and indication of the cross-section planes. (b) The green line represents the contact surface. The samples in the loaded zone were observed up to 1 mm from the contact surface. Distances further than 3 mm from the raceway surface were referred to as a non-loaded zone in this study.

2.2. Quantification Methodology

The morphology of the present NMIs was studied in detail, including their type, size, shape, orientation, bonding with bulk material, the possible presence of damage around NMIs, and distance with respect to the raceway. The samples were examined in two main zones. The first was to a depth of 1 mm below the raceway surface, which coincides with the zone of high rolling contact stresses in bearings [26,34]. The inclusions in the non-loaded zone were studied at a distance greater than 3 mm, where the stresses were insignificant in terms of inducing damage in the material. In this study, the size and shape of inclusions were characterized as follows. Firstly, the longest straight line connecting two points of the inclusion was identified as the first (principal) axis, and the longest line perpendicular to the first axis was identified as the second axis in the investigated 2D section, as shown in Figure 2. The first measure was the length of the longest axis, denoted L_{max} , and the length of the shortest axis was denoted L_{min} . The inclusion size was defined as the equivalent diameter.

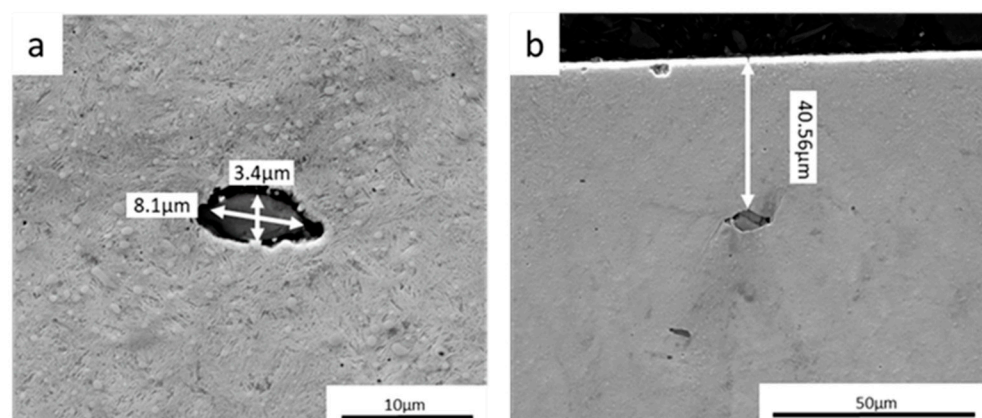


Figure 2. (a) Determination of the inclusion size. (b) Measurement of the distance from the raceway surface.

To investigate the influence of the shape of the inclusion on damage initiation, the aspect ratio (AR) was defined as the ratio between L_{max} and L_{min} . Additionally, the orientation of the inclusion was quantified as the smallest angle between the major axis and

the orientation of the image. It should be noted that the maximum value for the orientation of the inclusion was 90 degrees. These measurements provided a comprehensive characterization of the inclusions in the bearing steel. Furthermore, inclusion bonding with the bulk material was inspected based on the SEM images. The number density of the precipitates was quantified from BSE images. The quantification was performed over areas of $300 \times 300 \mu\text{m}^2$; for each sample, at least 10 areas were analyzed. The number density of inclusions in the two zones did not show variation, suggesting that they are homogeneously distributed throughout the sample.

2.3. Classification of Damage

This work distinguishes between inclusions forming “butterfly wings”, white etching cracks/white etching areas, and matrix cracks. In the investigation, WECs were observed with a WEA, and no WEA was present without a WEC. The EDS spectra and point analysis of WEA can be found in Appendix A, Figures A1 and A2. “Butterfly wings” are small features measured in tens of micrometers—these are wings-shaped white etching zones with a typical 45-degree orientation to the raceway surface. White etching cracks are recognized as cracks with shallower angles that typically exhibit a longer appearance than BWs, with an accompanying white etching area. Matrix cracks refer to cracks starting from inclusions in the bulk material without the formation of a WEA. These three different types of damage are shown in Figure 3. Some inclusions showed two types of damage: a matrix crack observed on the left side and a butterfly wing on the right (Figure 3b). Therefore, one inclusion may fall into two categories. The damage orientation is measured as the angle between the matrix crack/WEA/WEC and the orientation of the image.

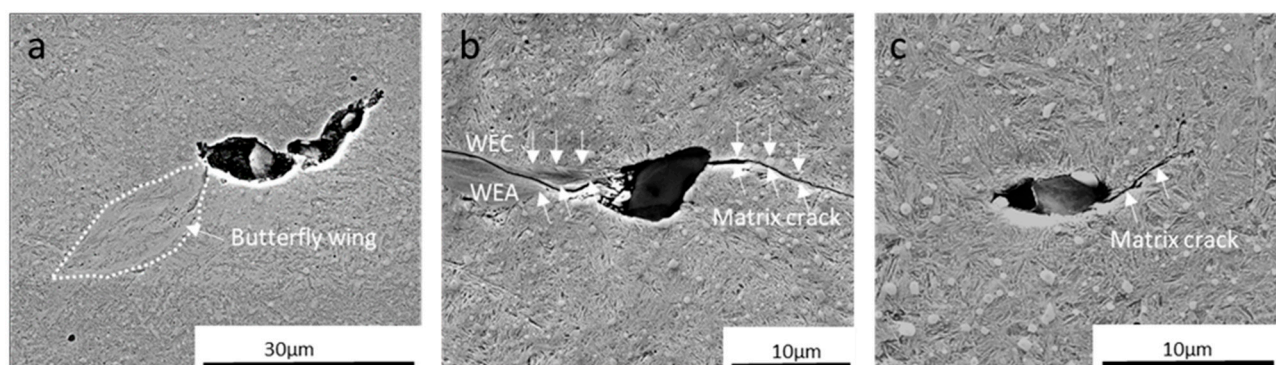


Figure 3. SEM-SE images of different types of damage observed in this study. (a) Appearance of butterfly wings. (b) White etching crack and white etching area. Arrows in the upper part point to the WEC, and arrows in the lower part indicate the WEA and (c) matrix crack.

3. Results

3.1. Characterization of Non-Metallic Inclusions in the Non-Loaded Zone

To understand the role of non-metallic inclusions in damage formation, we first investigated the non-metallic inclusions in the non-loaded zone. For that purpose, 70 inclusions were characterized at distances greater than 3 mm below the raceway surface. According to [23], this distance is sufficiently far below the loaded zone and, thus, will allow assessment of the attachment of inclusions to the bulk material in the initial state prior to the rolling. Microstructural alterations associated with WECs, BWs, and matrix cracks were not observed in this zone. Figure 4 illustrates nine inclusions in the non-loaded zone, showing that seven of them are marginally bonded to the martensitic matrix (a–g). Figure 4h,i depict inclusions that are intensely bonded to the bulk material, although there were slight indications of debonding (indicated in red). Figure 4 shows fragmented inclusions; this is rather unexpected due to the insignificant stress state. Fragmentation of inclusions can be associated with the ring rolling process. To verify that inclusion debonding is not caused by acid damage resulting from the etching process, the sample was repolished and

re-examined using SEM, as shown in Figure 5. It can be seen that debonding is still present within the material and was not altered due to the etching process. The average size of the inclusion, average length, aspect ratio, and the number density of the inclusions in the non-loaded zone are presented in Table 2. Most of the inclusions (77%) were MnS, and 88% of all inclusions were detached from the steel matrix. Given the fact that inclusions were already debonded prior to service, the question arises as to whether the initial stage of bonding plays a significant role in damage initiation and development, and consequently influences the bearing lifetime.

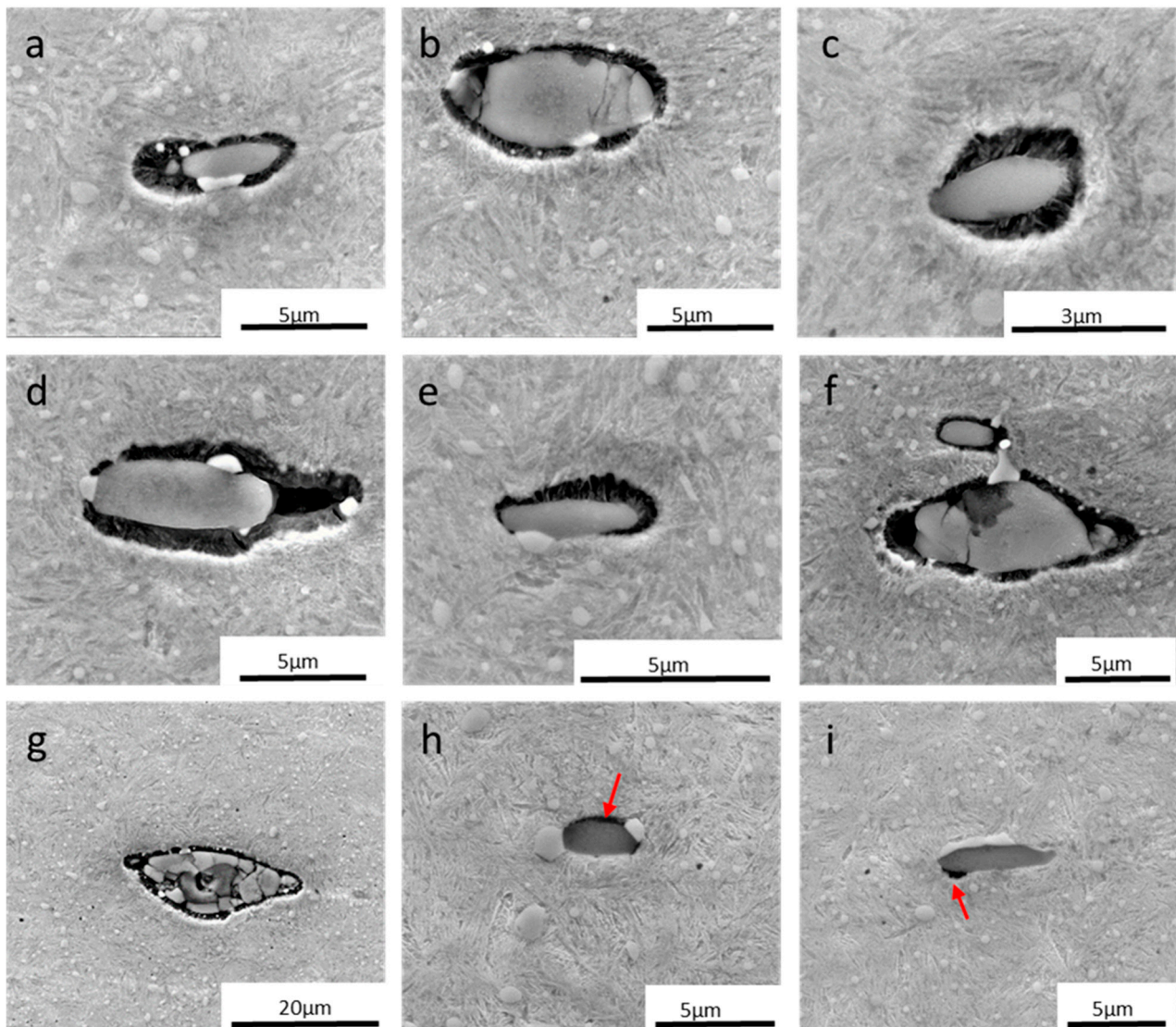


Figure 4. SEM-SE overview of the inclusions in the non-loaded zone. (a–f) Most of the inclusions shown (6 out of 9) are debonded from the bulk material. (g–i). Examples of bonded inclusions notwithstanding slight detachments indicated by red arrows.

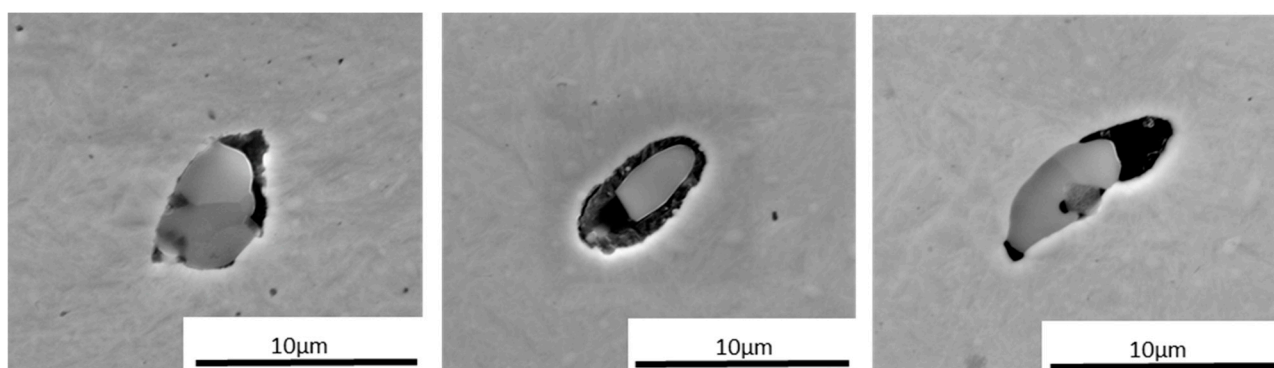


Figure 5. The SEM–BSE images of non-etched inclusions in the non-loaded zone confirm debonding in the absence of rolling contact fatigue.

Table 2. Characteristics of the inclusions in the non-loaded zone.

Average Size (μm)	Average Length (μm)	Average Aspect Ratio	Number Density (μm^{-2})
3.7	5.3	2.6	39

3.2. Characterization of Non-Metallic Inclusions in the Loaded Zone

The examination of the loaded zone revealed micro-damaged zones present as butterfly wings, matrix cracks, and white etching cracks. None of the BWs reached the raceway surface; they do not grow, and they do not create networks. Furthermore, WECs were found with a length of a few hundred microns, and no larger networks spanning millimeters in size were detected within the material, although connections between WECs were observed. Figure 6 shows inclusions and the damaged zones around them; the upper-left corner insertion indicates the distance from the raceway surface. It was found that damage is mainly present on the side of the inclusion detached from the bulk material. In addition, 72% of MCs and 73% of WECs started from the debonded side. The distance from the raceway surface varied from 22 to 676 μm , suggesting that debonding plays a role in the majority of the loaded zone rather than at the region of maximum shear stress, the latter of which was determined in [21,24]. Internal inclusion cracking is reported to be one of the forms of damage initiation [21,23,29]. In this study, a possible link between inclusion cracking and stress can be established since inclusion cracking peaked at 500 μm below the raceway surface. Under this distance, fewer cracked inclusions were observed. The inclusions with an equivalent diameter of 2–7 μm , determined as an average of major and minor inclusion axes, showed a larger tendency to crack. However, not all inclusions that developed BW/WEC/matrix cracks showed internal cracking.

Considering debonding as an important factor, all inclusions in the loaded zone were analyzed, and it was found that most of the inclusions (85%) in the loaded zone were detached from the steel matrix. The investigation of the inclusions in the non-loaded zone suggests that the load is not responsible for the debonding. This is most likely due to the different thermal expansion coefficients and/or strain incompatibilities being enhanced during the deformation processing. Moreover, the different thermal expansion coefficients of inclusions with the bulk material can result in the development of tensile and compressive residual stresses parallel to the normal inclusion–matrix interface. In addition, strain incompatibilities during the formation processing of the steel can result in the formation of cavities at the inclusion interface [42]. Given such a high number, it is suggested that size, shape, and chemical composition do not influence debonding of the inclusions.

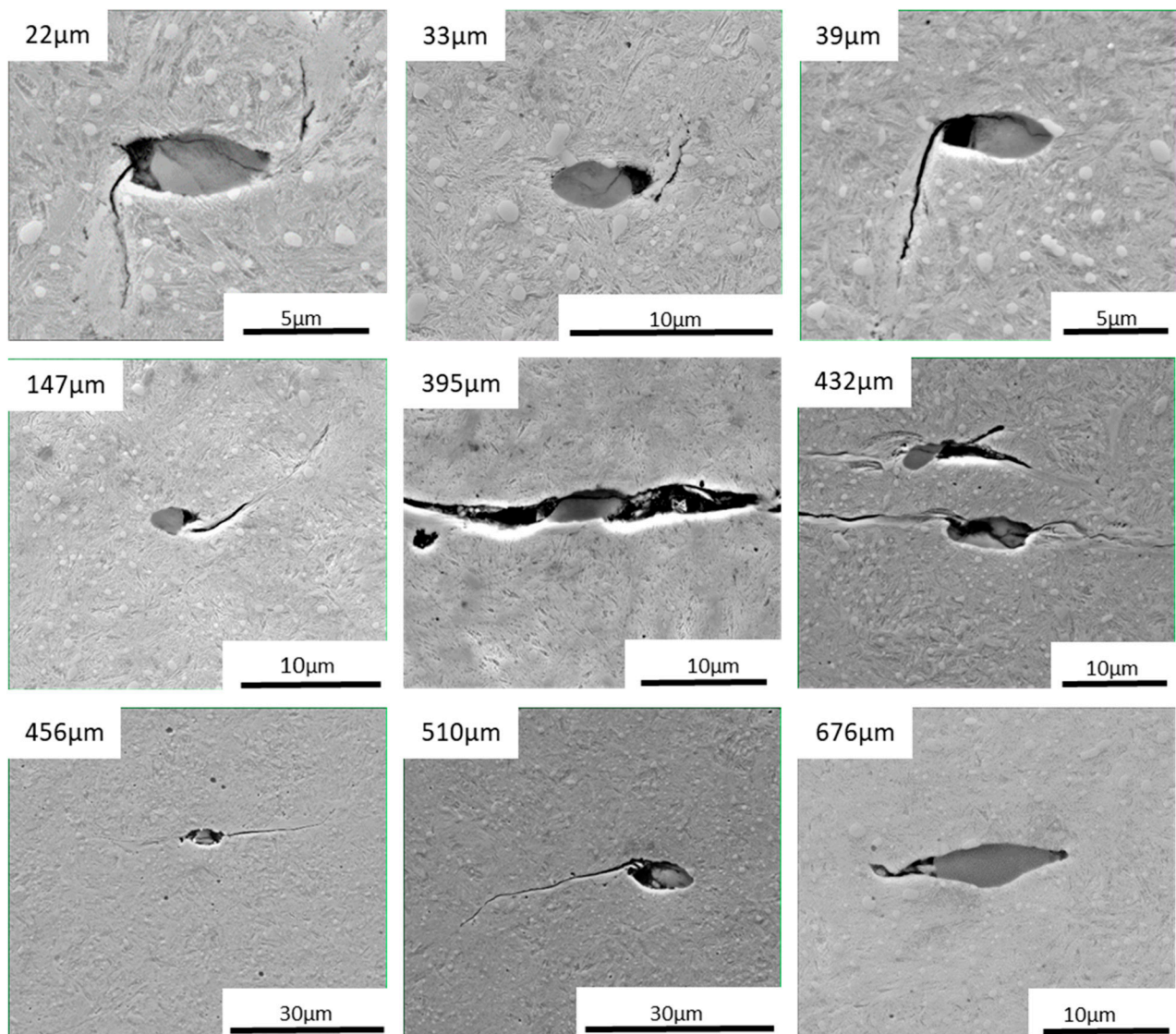


Figure 6. SEM-SE images of damage around inclusions in the loaded zone. The top-left number represents the distance from the raceway surface. The damage started on the side of the inclusion that was debonded from the bulk material. This is applicable for the wide range of distances (from 22 to 676 μm) from the raceway surface, suggesting that debonding plays a role in the entire loaded zone.

Table 3 presents the average size, average length, aspect ratio, and the number density of the studied inclusions in the loaded zone. The average size of inclusions did not vary between the loaded and non-loaded zone, and the average length and aspect ratio were slightly smaller in the loaded zone.

Table 3. Characteristics of the inclusions in the loaded zone.

Average Size (μm)	Average Length (μm)	Average Aspect Ratio	Number Density (μm^{-2})
3.5	4.7	2.1	41

3.3. Influence of the Chemical Composition and Shape

The chemical composition of the studied inclusions was analyzed with energy-dispersive spectroscopy. Only two types of inclusions were present in the studied bearing: pure MnS (77% of the studied database) and MnS with the addition of alumina (aluminum oxide). TiN and pure alumina were not detected in the material. Figure 7a,c show the

non-metallic inclusions captured by SEM, with white dots representing the locations of the EDS analysis. The corresponding EDS spectra of (a) and (c) are represented in (b) and (d), respectively. The different chemical composition of inclusions can also be observed in SEM figures; MnS is light grey without a different contrast, while two ‘particles’ (MnS + Al₂O₃) have different contrast, visible in (c). The percentage of the inclusions that caused a WEA is similar for both types: 34% for pure MnS and 37% for the MnS + Al₂O₃ type. Thus, our observations do not indicate a markable influence of the chemical composition of the inclusion on damage initiation.

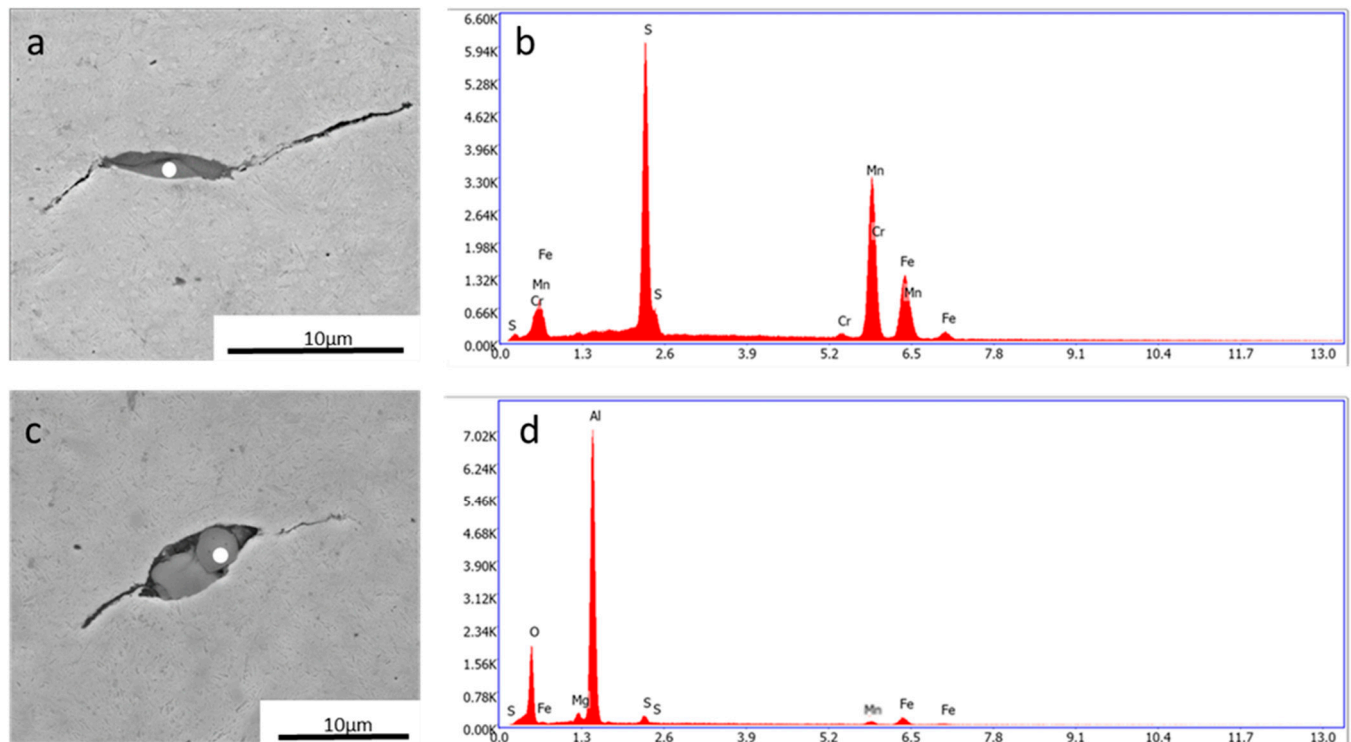


Figure 7. Types of inclusions present in this study. (a) SEM–SE figure of MnS inclusion; the white dot is where the spectra were taken. (b) EDS spectrum of the dot in (a). (c) MnS + Al₂O₃ inclusion type; this is also visible in the SEM figure, where contrast is present within different non-metallic compounds. (d) EDS spectrum of the white dot presented in (c).

The shape of inclusions can be defined as long or globular, depending on their aspect ratio. In line with reference [26], inclusions with an aspect ratio greater than three were considered as long and those with a ratio of less than three as globular. With this definition, the majority (85%) of studied inclusions are categorized as globular. In this work, no direct evidence on the shape of the inclusions in relation to damage development was found, indicated in Figure 7b.

3.4. Size of the Inclusions in Relation to Damage Development

The non-metallic inclusion size is of primary importance concerning fatigue life. Neishi et al. [25] correlated MnS inclusion length with rolling contact fatigue (RCF) life, indicating that the reduction in inclusion length is one of the crucial factors to improve RCF life. To investigate what sizes of inclusions gave rise to a microstructural alteration in bearing steel, their length and width were measured, from which their equivalent diameter was derived. In addition, we analyzed the length of the non-metallic inclusions and the relation to damage initiation. Most inclusions fell into the range of 1–10 μm. This result shows that inclusions in the present study were, on average, smaller than those reported by other authors (8–16 μm and 5–30 μm, respectively) [21,23], while the dimensions fit

with the observations in [24,26]. Figure 8 shows the depth versus size, aspect ratios, and max length of the inclusions; red dots are the inclusions that initiated damage, and blue inclusions are without damage. The equivalent diameter of the inclusions across depth suggests that they are randomly distributed throughout the sample (cf. Figure 8a). In Figure 8b, we observe the relationship between inclusion length and the percentage of initiated MCs and WECs. The damage percentage was determined by categorizing all non-metallic inclusions in the loaded zone based on their size per 1 micron, such as 0–1 micron intervals, 1–2 microns, 2–3 microns, and so on. Subsequently, the total number of non-metallic inclusions in the specific zone and the count of damage initiated by these inclusions were established. Inclusions measuring up to 2 μm exhibit a low probability of damage, less than 30%. However, as the inclusion length reaches 3 μm and beyond, there is a significant rise in damage initiation. The greatest percentages of damage occur at inclusion lengths of 8 μm , with 66% for MC and 56% for WEC. A similar observation as in Figure 8a is valid for the aspect ratio, maximum length of the inclusions (cf. Figure 8c), and maximum length across the depth of the sample (cf. Figure 8d).

3.5. Variation of Damage Morphology as a Function of Stresses

In this section, the microstructural features of butterfly wings and white etching cracks were evaluated. Some authors referred to both as a non-linked phenomenon [23], while others see the BWs as a precursor for WECs [26,35,47,48]. It is reported that WECs appear to develop in parallel or branching patterns without following any particular maximum shear stress directions [49]. In this study, BWs were found down to 200 μm below the surface, with the majority of them being closer than 100 μm to the surface. The inclusions leading to WECs were located within a band of 200–500 μm below the surface, which is assumed to be the zone that experienced high rolling contact stresses. It is widely accepted that BWs initiate within the angle of 45 degrees with respect to the over-rolling surface. Moreover, given the depth below the surface, WECs cannot initiate at these angles as the shear stresses are not the same as in the zone up to 200 μm . Of course, these numbers correspond to this particular bearing, given its particular loading history. The orientation of the inclusions in relation to the distance below the surface is presented in Figure 9a. Inclusions tend to have a lower orientation angle smaller than 30 degrees. The orientations of microstructural alterations across the depth of the sample are presented in Figure 9b. Most of the alterations up to 200 μm are oriented close to 45 degrees, and the angles become shallower as the inclusion depth increases.

To illustrate potential damage orientations, examples of microstructural alteration are shown in Figure 10. A typical butterfly wing pattern of 45 degrees is depicted in Figure 10a, where both sides of the non-metallic inclusions developed BWs. The distance of this inclusion was very close to the raceway surface (22 μm); however, no connection of the crack to the surface was observed. Further away from the surface (345 μm), microstructural alterations propagate at shallower angles (cf. Figure 10b). Here, cracks also developed from both sides of the inclusions; cracks are longer than BWs, and the altered zone is broader in this zone. On the contrary, at distances greater than 500 μm , cracks were typically evolving from only one side of the inclusions, and a very thin WEA was observed around them (Figure 10c). These findings were consistent throughout this investigation and supported the hypothesis that WECs are an extension of BWs.

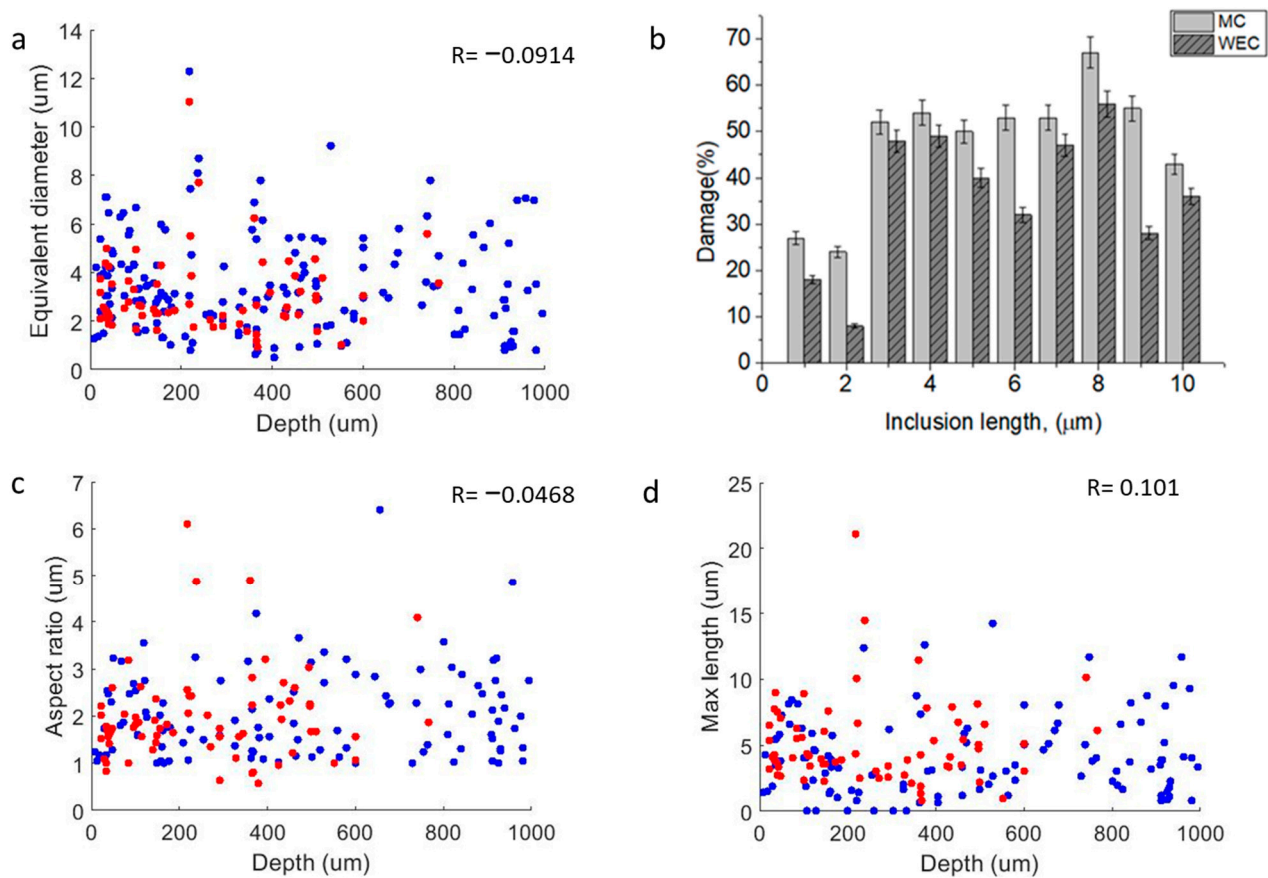


Figure 8. (a) Distribution of inclusion size across depth. (b) Percentage of initiated MCs/WECs in correspondence with inclusion length. (c) Maximum length of inclusions across depth. (d) Aspect ratio across the depth. Red represents inclusions that initiated damage, and blue indicates inclusions without damage.

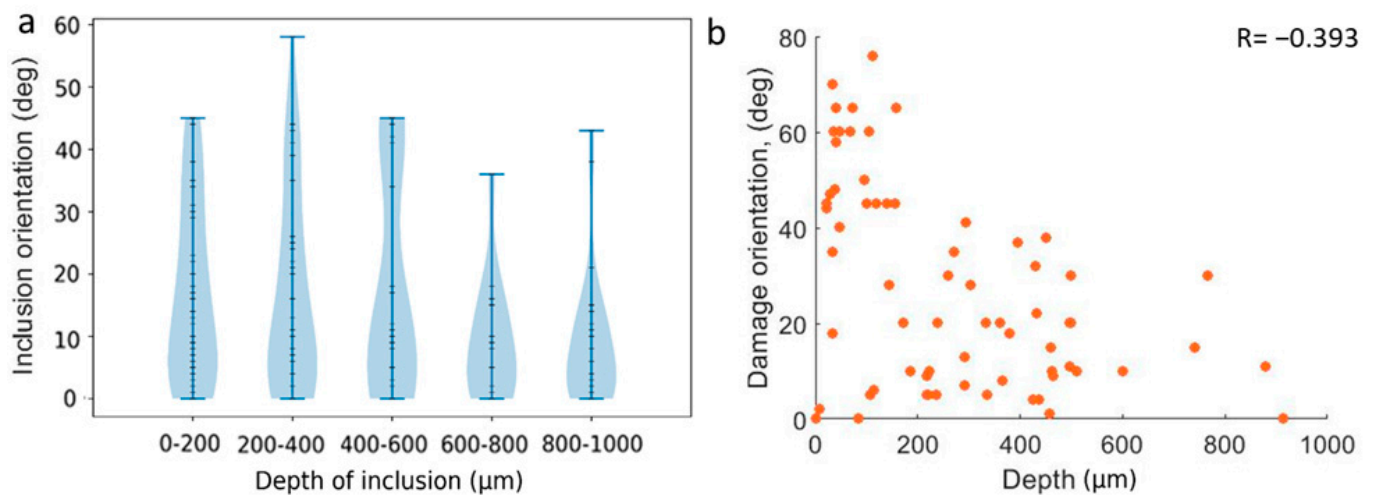


Figure 9. (a) Inclusion orientation across the depth. (b) Average angle of damage in relation to depth.

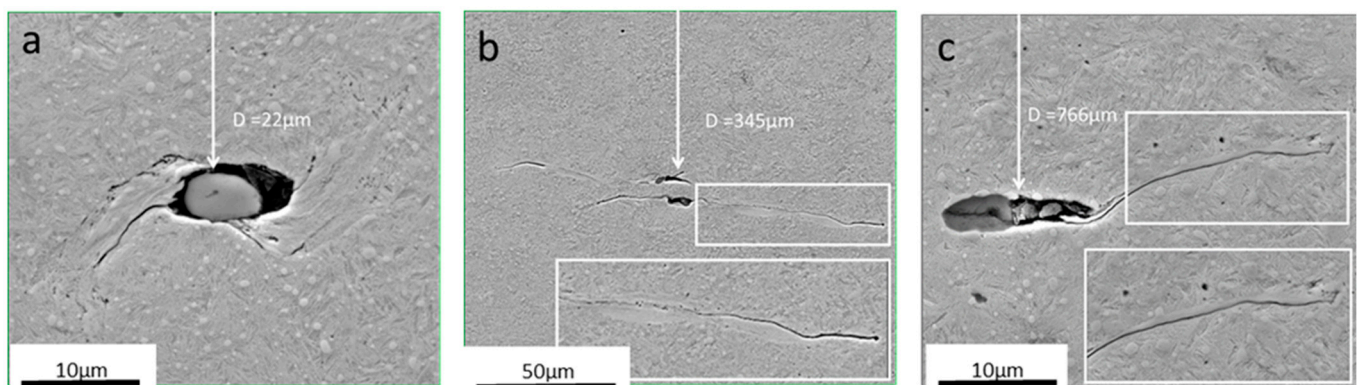


Figure 10. Development of damage at the depth of the sample. (a) Orientation of butterfly wing, (b) Orientation of white etching cracks, (c) orientation of matrix crack.

Figure 11 shows the occurrence of white etching cracks and matrix cracks across the depth of the sample and their corresponding length. The average value of multiple inclusions length per 100 μm is shown. A clear trend can be observed with a high number of cracks (matrix cracks and white etching cracks) up to 500 microns, followed by a steep decline, with only one matrix crack present at a distance between 900 and 1000 μm . Moreover, the average length of inclusions varied from 4 to 6.5 μm , up to 500 μm below the raceway surface, and at distances greater than 500 μm longer (around 9 μm), inclusions initiated a matrix crack. Furthermore, the size of white etching areas changes as the distance from the raceway surface increases. Within a range from the raceway surface up to 200 μm , the length of the white etching varies from 10 to 30 μm , with one exception where a length of 100 μm was measured. The longest white etching cracks (in a range of 100 μm) were found in a zone between 200 and 500 μm . At larger distances within the range of 500–1000 μm , shorter white etching cracks with an average length of 30 microns were observed. This indicates the influence of stresses, i.e., at greater distances (>500 μm), longer inclusions are required for damage initiation.

3.6. Length of the WEC in Relation to the Size of the Inclusions

In this section, the lengths of the inclusions that caused the longest WECs in this bearing were analyzed to disclose the main factor for the damage initiation from the size, shape, angle, or debonding. However, it is important to note that all observations were conducted in two-dimensional sections. WEC networks were relatively short (up to 160 μm)—as such, the inclusions related to WECs were considered to be the initiation locations of WECs rather than the propagating WECs being incidentally connected to the inclusion. Figure 12 shows the length of WECs, the length of inclusions, and the orientation of the inclusions to the raceway surface. The lengths of the inclusions that initiated the longest WECs were in the range of 2–5 μm ; most of them (90%) ranged from 350–500 μm below the raceway surface. The orientations of the inclusions varied from 3 to 44 degrees with respect to the over-rolling direction, suggesting that there is no strong link between the inclusion orientation and the initiation of damage. The majority (85%) of inclusions showing WECs were debonded from the steel matrix. In this case, the shape was not considered because most inclusions (85%) in the studied bearing were globular. The chemical composition of the inclusions that initiated long WECs was, in most cases, (87.5%) pure manganese sulfide without the addition of calcium, magnesium, or alumina. It should be noted that the percentage of so-called multi-phase inclusions was low throughout the bearing at only 23%. Based on this observation, it is suggested that small (2–5 μm) debonded MnS inclusions caused damage initiation.

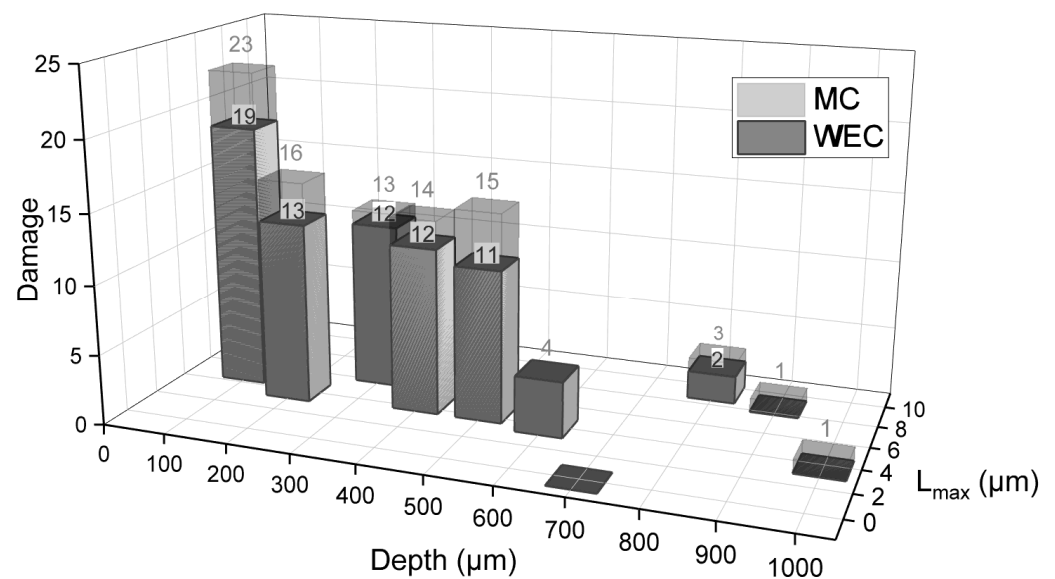


Figure 11. WEC and matrix crack initiation in relation to inclusion size and distance from the raceway surface.

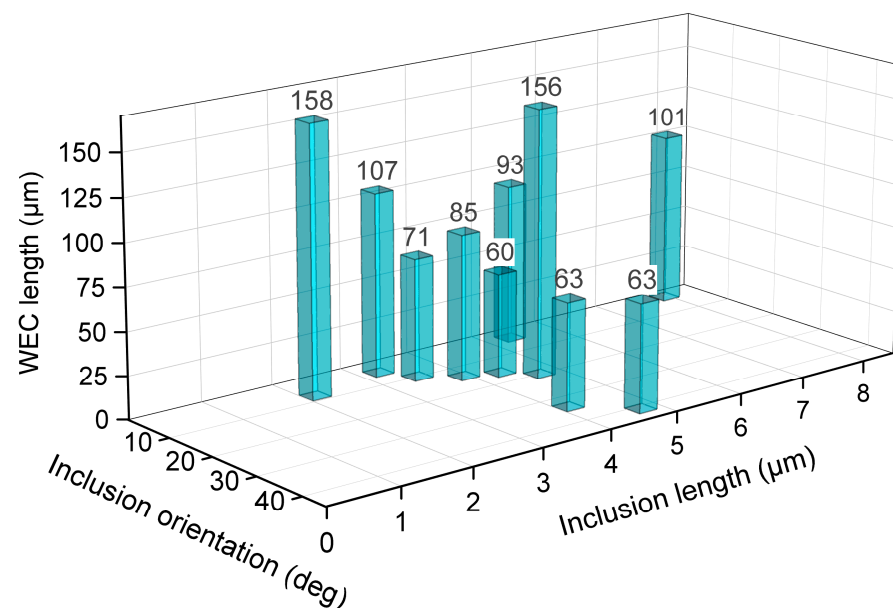


Figure 12. Overview of the longest WECs observed in the studied bearing. The length of WECs was plotted to the corresponding length of the inclusion that initiated WEC and the inclusion orientation to the over-rolling direction.

4. Discussion

The comparison between inclusions in the loaded and non-loaded zones showed similar average sizes, chemical compositions, aspect ratios, number densities, and debonding degrees from the steel matrix, indicating that they are randomly distributed within the material and not altered by the steel-making process and/or by the presence of loading. White etching cracks and butterfly wings were found initiated around non-metallic inclusions. Furthermore, microstructural alterations were observed in the zone subjected to high stresses, specifically within the range of inclusion lengths from 4 to 6.5 μm. As the stresses decreased, there was a transition towards longer inclusions that served as the initiation points for cracks (Figure 11). A similar trend was observed for the length of WECs; the longest WECs were observed at a depth range of 200 up to 500 μm. Furthermore, the

lengths of inclusions that initiated the longest WECs were from 2 to 5 μm . The literature review points to the multi-phase inclusions [20] and the density of the inclusions [26]. Gould et al. [20] reported that multi-phase inclusions (mixture of aluminum, manganese, and sulfur) are more prone to develop damage than pure MnS inclusions. However, in this work, no evidence was found to confirm the importance of the NMI's chemical composition. The main factor found in our study for inclusion to act as a damage initiator is the initial stage of the bonding of a non-metallic inclusion with the steel matrix. In the literature on white etching cracks, it is widely debated whether butterfly wings are precursors for white etching cracks. According to Lewis and Tomkins [50], butterflies can be classified into two categories: "propagating butterflies", which can initiate WEC networks, and "non-propagating butterflies", which refer to cracks that stop at the inclusion neighborhood. Bruce et al. [23] proposed that a WEA originates from these inclusions at a different angle (compared to the typical 30–50 degree angle of classic butterflies) and referred to WECs as WEC-initiating inclusions. We observed that butterfly wings were closer to the raceway surface, up to 100 μm , usually at an angle of 30–50 degrees with respect to the over-rolling surface. In addition, butterfly wings did not tend to reach the raceway surface or create a network. On the other hand, white etching cracks were present in the zone from 200 to 500 μm below the raceway surface and, subsequently, tended to connect. The initiation angles of BWs and WECs also differ depending on the distance of the inclusion from the over-rolling surface. As shown in Figure 9b, the angle of WEC development is close to 0 degrees at distances larger than 200 μm from the rolling surface. The damage of WECs also starts from non-metallic inclusions, this time in the high-loaded zone, where the stresses reached the peak. In contrast to the BWs, they do tend to connect at the angle of 10–20 degrees, which can subsequently cause spalling of the raceway surface over time. These findings are consistent with the results reported in [21,23].

The authors in [23,51] reported that NMI debonding is the first stage of damage and is considered to be the mechanism responsible for damage development. However, in the current work, we found the existence of a very large fraction (88%) of debonded inclusions in the non-loaded zone of the bearing. Hence, it can be hypothesized that the debonded inclusions already existed in the microstructure of the bearing before their exploitation. Most likely, this debonding might be a consequence of quenching and/or differences in thermal expansion coefficients of the matrix and the inclusion [42]. If these inclusions are located in the heavily loaded zone with high Hertzian stresses, they tend to develop voids further until a certain threshold is reached when the local stress concentration is too high to accommodate; thus, matrix cracks appear as a way of stress relief.

The microstructural observation that proves the proposed formation mechanism of the crack initiation in the bulk material is shown in Figure 13. The debonded inclusion is located in the loaded zone (up to 1 mm from the raceway surface). As the rolling cycles occur, local stress concentration develops around the debonded area, as shown in Figure 13a. Over successive rolling cycles, the stress levels increase, resulting in the formation of voids (regions with white arrows in Figure 13). These voids serve as regions of local high-stress concentration, which eventually develop microcracks into bulk material as means of stress relief. Figure 13b shows an inclusion with a fully developed butterfly wing on the right-hand side, while the left side only has a small indication of the crack in the bulk material.

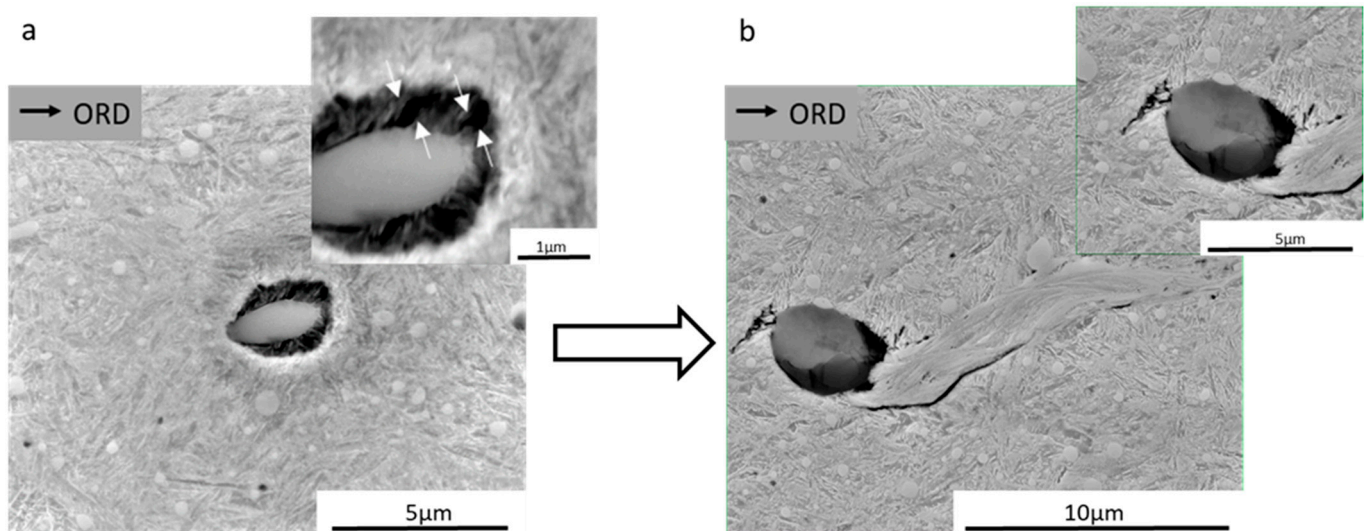


Figure 13. Proposed damage development. ORD represents the over-rolling direction. (a) Non-metallic inclusion in the non-loaded zone. (b) Once the non-metallic inclusion located in the loaded zone experiences rolling cycles, damage first initiates in the debonded zone and initiates a crack in the bulk material as a way of stress relief.

Comparing the microstructural alterations in different zones, earlier postulated mechanisms about crack rubbing and severe plastic deformation can be confirmed. A graphical representation of the proposed hypothesis is shown in Figure 14. In zone Ia, only individually present BWs were observed, which had a typical 45-degree propagation on either side of the non-metallic inclusion. In zone Ib of Figure 14, most of the WECs consisted of cracks propagating left and right from the non-metallic inclusions with a significantly thick WEA developed in the vicinity of the WEC. In zone II, most cracks appear only on one side of the non-metallic inclusions and the accompanying WEA was thinner than in zone Ib. These findings are in line with the previously proposed mechanism [35,52]. Indications of severe plastic deformation can be derived by comparing zones Ib and II. Zone II (where the stresses due to over-rolling contact are less pronounced) had a less deformed area around the WEC. Lower stresses mean that crack face rubbing is less intense; consequently, less WEAs are formed.

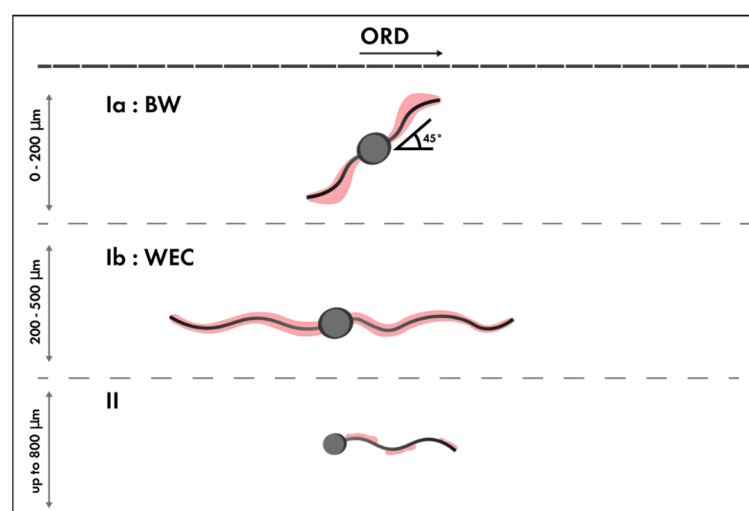


Figure 14. Schematic representation of the appearance of microstructural alteration with respect to the angle of initiation and depth below the raceway surface.

5. Summary and Conclusions

The present work studies a failed bearing collected from the field after unknown hours of operation. Non-metallic inclusions were catalogued according to their depth below the raceway surface, their chemical composition, their angle with respect to the raceway surface, the damage around them, their size, their shape, and their bonding with the surrounding matrix. The main findings for the investigated bearing are as follows:

The investigation confirmed that BWs and WECs were formed around non-metallic inclusions. WECs were present at shallower angles and greater distances below the raceway surface than BWs.

The appearance of the microstructural alteration was categorized across the depth below the raceway surface. No BWs were observed at distances greater than 200 μm . The WECs at distances of 200–500 μm developed a thick deformed zone. Observations at distances exceeding 500 μm revealed the presence of cracks exclusively on one side of the inclusions, accompanied by a thin layer of WEAs. This suggests that the mechanism for WEA formation is severe plastic deformation.

In this investigation, the longest WECs originated from inclusions with a length ranging from 2 to 5 μm .

The initial stage of bonding of the non-metallic inclusions to the steel matrix is an important parameter to consider for damage initiation. This can be attributed to the debonded zone acting as a void. When the void reaches a critical size due to the elevated local stresses, it will relieve the stress by generating a crack originating from the inclusion within the steel matrix.

Despite the previous work on this topic, we could not confirm that the NMI chemical composition was important for damage initiation. In this work, the MnS inclusion containing the alumina particles at the top did not seem to generate more damage than the pure MnS inclusions.

Other factors such as shape, angle, and fragmentation are of secondary importance in the development of damage in the investigated bearing.

Given the abovementioned findings, it should be noted that while size and chemical composition are significant factors in determining damage, the separation of inclusions from the steel matrix prior to the service can also significantly affect the bearing's lifespan. Therefore, it is essential to consider all parameters when evaluating the cause of bearing failure.

Author Contributions: Conceptualization, K.N. and R.H.P.; methodology, K.N., T.D., K.V. and R.H.P.; validation, J.D.W., G.R. and S.H.; formal analysis, K.N. and J.D.W.; investigation, K.N., J.D.W. and G.R.; data curation, K.N., J.D.W., G.R. and S.H.; writing—original draft, K.N.; writing—review and editing, K.N., S.H., T.D., K.V. and R.H.P.; visualization, K.N., J.D.W. and S.H.; supervision, T.D., K.V. and R.H.P.; funding acquisition, R.H.P. All authors have read and agreed to the published version of the manuscript.

Funding: The authors gratefully acknowledge the financial support provided by the MaDurOS program from VLAIO (Flemish Agency for Innovation and Entrepreneurship) and SIM (Strategic Initiative Materials) through project SBO MaSiWEC (HBC.2017.0606).

Data Availability Statement: Not applicable.

Conflicts of Interest: The authors declare no conflict of interest. The funders had no role in the design of the study; in the collection, analyses, or interpretation of data; in the writing of the manuscript, or in the decision to publish the results.

Appendix A

Figures A1 and A2 represent the energy EDS analysis over the white etching area. Figure A1a shows the SEM–SE image over the area of interest. Depletion of chromium carbides in the white etching area is visible from the chromium map in Figure A1b. Sulfide and manganese compositions of the non-metallic inclusion are shown in Figure A1c,d,

respectively. The spot EDS analysis shows the same area as in Figure A1. The altered zone (white etching area) is more visible in the backscattered image in Figure A2a. The spectra from the inclusion, carbide, martensitic matrix, and white etching area are represented in Figure A2b–e, respectively.

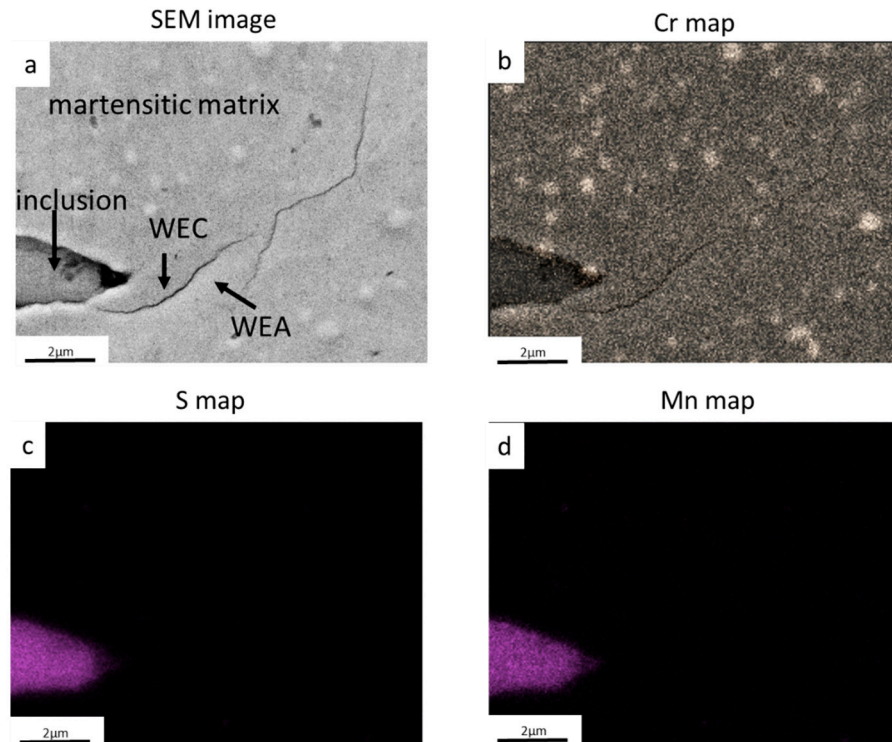


Figure A1. EDS spectrum on white etching area and inclusion. (a) SEM–SE image on the area of interest. (b) Chromium map. (c) Sulfur map. (d) Manganese map.

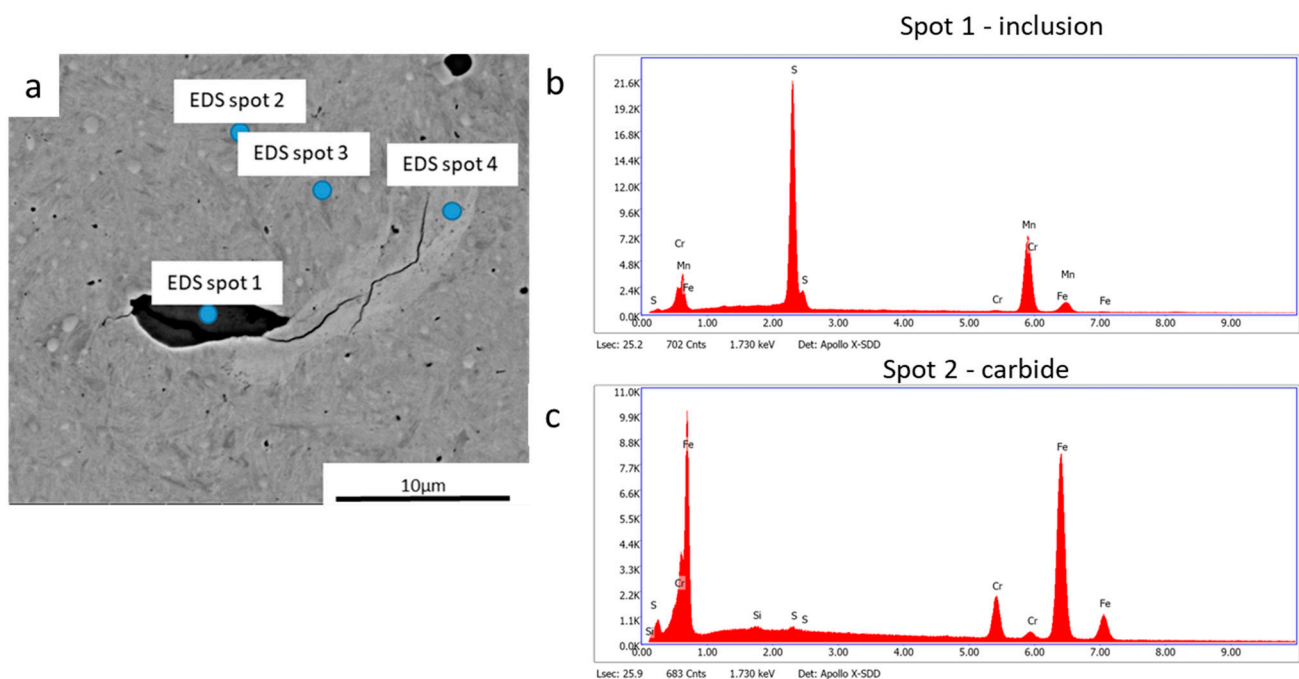


Figure A2. *Cont.*

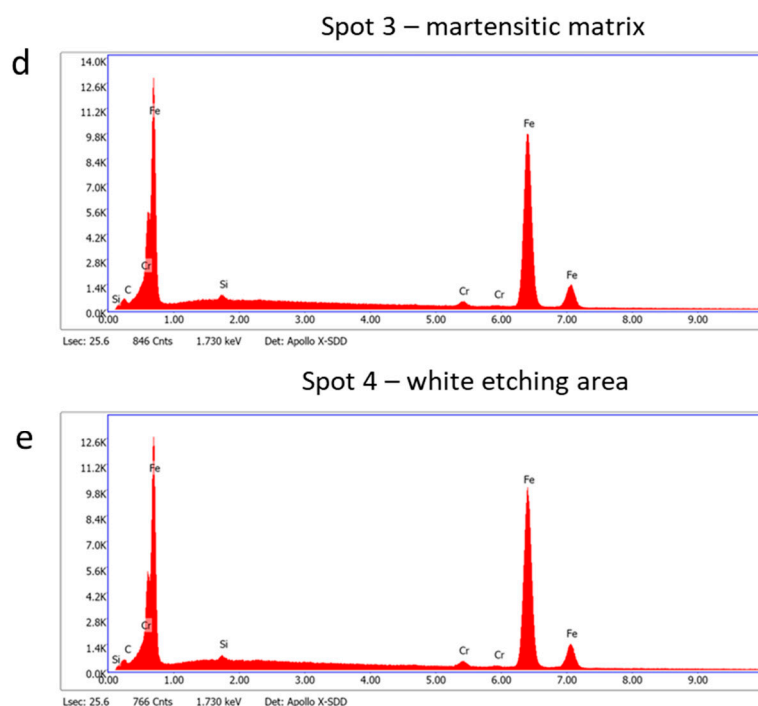


Figure A2. EDS spot analysis. (a) SEM–BSE area of interest; blue dots represent the location where the spectra analysis was taken. (b) Inclusion. (c) Chromium-rich carbide. (d) Martensitic matrix. (e) White etching area.

References

- Renewable Energy Targets [Online]. Available online: https://energy.ec.europa.eu/topics/renewable-energy/renewable-energy-directive-targets-and-rules/renewable-energy-targets_en (accessed on 30 April 2023).
- Sheng, S.; Veers, P. Wind Turbine Drivetrain Condition Monitoring—An Overview. 2011. Available online: <https://nrel.gov/docs/fy12osti/50698.pdf> (accessed on 2 May 2023).
- Tusar, M.I.H.; Sarker, B.R. Developing the optimal vessel fleet size and mix model to minimize the transportation cost of offshore wind farms. *Ocean Eng.* **2023**, *274*, 114041. [CrossRef]
- Gearbox Reliability Database. Available online: <https://grd.nrel.gov/stats> (accessed on 12 February 2023).
- Stadler, K.; Lai, J.; Vegter, R.H. A Review: The Dilemma with Premature White Etching Crack (WEC) Bearing Failures. *Bear. Steel Technol. Adv. Steel Technol. Roll. Bear.* **2014**, *10*, 1580. [CrossRef]
- Paladugu, M.; Lucas, D.R.; Hyde, R.S. Effect of lubricants on bearing damage in rolling-sliding conditions: Evolution of white etching cracks. *Wear* **2018**, *398–399*, 165–177. [CrossRef]
- Kürten, D.; Khader, I.; Raga, R.; Casajús, P.; Winzer, N.; Kailer, A.; Spallek, R.; Scherge, M. Hydrogen assisted rolling contact fatigue due to lubricant degradation and formation of white etching areas. *Eng. Fail. Anal.* **2019**, *99*, 330–342. [CrossRef]
- Spille, J.; Wranik, J.; Barteldes, S.; Mayer, J.; Schwedt, A.; Zürcher, M.; Lutz, T.; Wang, L.; Holweger, W. A study on the initiation processes of white etching cracks (WECs) in AISI 52100 bearing steel. *Wear* **2021**, *477*, 203864. [CrossRef]
- Gould, B.; Demas, N.; Erck, R.; Lorenzo-Martin, M.C.; Ajayi, O.; Greco, A. The effect of electrical current on premature failures and microstructural degradation in bearing steel. *Int. J. Fatigue* **2021**, *145*, 106078. [CrossRef]
- Wranik, J.; Holweger, W.; Lutz, T.; Albrecht, P.; Reichel, B.; Wang, L. A Study on Decisive Early Stages in White Etching Crack Formation Induced by Lubrication. *Lubricants* **2022**, *10*, 96. [CrossRef]
- Tung, P.Y.; McEniry, E.; Herbig, M. The role of electric current in the formation of white-etching-cracks. *Philos. Mag.* **2020**, *101*, 59–76. [CrossRef]
- Steinweg, F.; Mikitisin, A.; Oezel, M.; Schwedt, A.; Janitzky, T.; Hallstedt, B.; Broeckmann, C.; Mayer, J. Formation of White Etching Cracks under electrical current flow—Influence of load, slip and polarity. *Wear* **2022**, *504–505*, 204394. [CrossRef]
- Loos, J.; Bergmann, I.; Goss, M. Influence of High Electrical Currents on WEC Formation in Rolling Bearings. *Tribol. Trans.* **2021**, *64*, 708–720. [CrossRef]
- Oezel, M.; Schwedt, A.; Janitzky, T.; Kelley, R.; Bouchet-Marquis, C.; Pullan, L.; Broeckmann, C.; Mayer, J. Formation of white etching areas in SAE 52100 bearing steel under rolling contact fatigue—Influence of diffusible hydrogen. *Wear* **2018**, *414–415*, 352–365. [CrossRef]
- López-Uruñuela, J.F.; Fernández-Díaz, B.; Pinedo, B.; Aguirrebeitia, J. Early stages of subsurface crack and WEC formation in 100Cr6 bearing steel under RCF and hydrogen influence. *Int. J. Fatigue* **2022**, *155*, 106587. [CrossRef]

16. Liang, X.Z.; Rivera-Díaz-del-Castillo, P.E.J. Hydrogen-accelerated white etching area formation in bearings under rolling contact fatigue. *Int. J. Fatigue* **2022**, *159*, 106753. [\[CrossRef\]](#)
17. Liang, X.Z.; Zhao, G.H.; Owens, J.; Gong, P.; Rainforth, W.M.; Rivera-Díaz-del-Castillo, P.E.J. Hydrogen-assisted microcrack formation in bearing steels under rolling contact fatigue. *Int. J. Fatigue* **2020**, *134*, 105485. [\[CrossRef\]](#)
18. Andric, P.; Restrepo, S.E.; Lai, J.; Venner, C.H.; Vegter, E. Mechanistic driving force for martensite decay in rolling contact fatigue. *Tribol. Int.* **2023**, *184*, 108470. [\[CrossRef\]](#)
19. Johnson, K.L. *Contact Mechanics*; Cambridge University Press: Cambridge, UK, 1987.
20. Gould, B.; Greco, A.; Stadler, K.; Vegter, E.; Xiao, X. Using advanced tomography techniques to investigate the development of White Etching Cracks in a prematurely failed field bearing. *Tribol. Int.* **2017**, *116*, 362–370. [\[CrossRef\]](#)
21. Al-Tameemi, H.A.; Long, H.; Dwyer-Joyce, R.S. Initiation of sub-surface micro-cracks and white etching areas from debonding at non-metallic inclusions in wind turbine gearbox bearing. *Wear* **2018**, *406–407*, 22–32. [\[CrossRef\]](#)
22. Richardson, A.D.; Evans, M.H.; Wang, L.; Wood, R.J.K.; Ingram, M.; Meuth, B. The Evolution of White Etching Cracks (WECs) in Rolling Contact Fatigue-Tested 100Cr6 Steel. *Tribol. Lett.* **2018**, *66*, 6. [\[CrossRef\]](#)
23. Bruce, T.; Rounding, E.; Long, H.; Dwyer-Joyce, R.S. Characterisation of white etching crack damage in wind turbine gearbox bearings. *Wear* **2015**, *338–339*, 164–177. [\[CrossRef\]](#)
24. Evans, M.H.; Richardson, A.D.; Wang, L.; Wood, R.J.K.; Anderson, W.B. Confirming subsurface initiation at non-metallic inclusions as one mechanism for white etching crack (WEC) formation. *Tribol. Int.* **2014**, *75*, 87–97. [\[CrossRef\]](#)
25. Neishi, Y.; Makino, T.; Matsui, N.; Matsumoto, H.; Higashida, M.; Ambai, H. Influence of the inclusion shape on the rolling contact fatigue life of carburized steels. *Metall. Mater. Trans. A Phys. Metall. Mater. Sci.* **2013**, *44*, 2131–2140. [\[CrossRef\]](#)
26. Evans, M.; Richardson, A.D.; Wang, L.; Wood, R.J.K. Serial sectioning investigation of butterfly and white etching crack (WEC) formation in wind turbine gearbox bearings. *Wear* **2013**, *302*, 1573–1582. [\[CrossRef\]](#)
27. Danielsen, H.K.; Guzmán, F.G.; Dahl, K.V.; Li, Y.J.; Wu, J.; Jacobs, G.; Burghardt, G.; Fæster, S.; Alimadadi, H.; Goto, S.; et al. Multiscale characterization of White Etching Cracks (WEC) in a 100Cr6 bearing from a thrust bearing test rig. *Wear* **2017**, *370–371*, 73–82. [\[CrossRef\]](#)
28. Vegter, E.; Krock, H.; Kadin, Y.; Ocelík, V. Nonmetallic Inclusion Bonding in Bearing Steel and the Initiation of White-Etching Cracks. *Bear. Steel Technol. 11th Vol. Adv. Steel Technol. Roll. Bear.* **2017**, *11*, 519–532. [\[CrossRef\]](#)
29. Al-Bedhany, J.H.; Long, H. Microscopic investigation of subsurface initiated damage of wind turbine gearbox bearings. *J. Phys. Conf. Ser.* **2018**, *1106*, 012029. [\[CrossRef\]](#)
30. Bruce, T.; Long, H.; Slatter, T. Formation of white etching cracks at manganese sulfide (MnS) inclusions in bearing steel due to hammering impact loading. *Wind Energy* **2016**, *19*, 1903–1915. [\[CrossRef\]](#)
31. Hiraoka, K.; Nagao, M.; Isomoto, T. Study on Flaking Process in Bearings by White Etching Area Generation. *J. ASTM Int.* **2006**, *3*, 234–240. [\[CrossRef\]](#)
32. Grabulov, A.; Ziese, U.; Zandbergen, H.W. TEM/SEM investigation of microstructural changes within the white etching area under rolling contact fatigue and 3-D crack reconstruction by focused ion beam. *Scr. Mater.* **2007**, *57*, 635–638. [\[CrossRef\]](#)
33. Osterlund, R.; Vingsbo, O.; Vincent, L.; Guiraldenq, P. Butterflies in Fatigued Ball Bearings—Formation Mechanisms and Structure. *Scand. J. Metall.* **1982**, *11*, 23–32.
34. Evans, M.H.; Walker, J.C.; Ma, C.; Wang, L.; Wood, R.J.K. A FIB/TEM study of butterfly crack formation and white etching area (WEA) microstructural changes under rolling contact fatigue in 100Cr6 bearing steel. *Mater. Sci. Eng. A* **2013**, *570*, 127–134. [\[CrossRef\]](#)
35. Morsdorf, L.; Mayweg, D.; Li, Y.; Diederichs, A.; Raabe, D.; Herbig, M. Moving cracks form white etching areas during rolling contact fatigue in bearings. *Mater. Sci. Eng. A* **2020**, *771*, 138659. [\[CrossRef\]](#)
36. Mayweg, D.; Morsdorf, L.; Wu, X.; Herbig, M. The role of carbon in the white etching crack phenomenon in bearing steels. *Acta Mater.* **2021**, *203*, 116480. [\[CrossRef\]](#)
37. Li, Y.J.; Herbig, M.; Goto, S.; Raabe, D. Atomic scale characterization of white etching area and its adjacent matrix in a martensitic 100Cr6 bearing steel. *Mater. Charact.* **2017**, *123*, 349–353. [\[CrossRef\]](#)
38. Kang, J.H.; Hosseinkhani, B.; Williams, C.A.; Moody, M.P.; Bagot, P.A.J.; Rivera-Díaz-Del-Castillo, P.E.J. Solute redistribution in the nanocrystalline structure formed in bearing steels. *Scr. Mater.* **2013**, *69*, 630–633. [\[CrossRef\]](#)
39. Šmelova, V.; Schwedt, A.; Wang, L.; Holweger, W.; Mayer, J. Microstructural changes in White Etching Cracks (WECs) and their relationship with those in Dark Etching Region (DER) and White Etching Bands (WEBs) due to Rolling Contact Fatigue (RCF). *Int. J. Fatigue* **2017**, *100*, 148–158. [\[CrossRef\]](#)
40. Greco, A.; Sheng, S.; Keller, J.; Erdemir, A. Material wear and fatigue in wind turbine Systems. *Wear* **2013**, *302*, 1583–1591. [\[CrossRef\]](#)
41. Da Costa E Silva, A.L.V. The effects of non-metallic inclusions on properties relevant to the performance of steel in structural and mechanical applications. *J. Mater. Res. Technol.* **2019**, *8*, 2408–2422. [\[CrossRef\]](#)
42. Bhadeshia, H.K.D.H. Steels for bearings. *Prog. Mater. Sci.* **2012**, *57*, 268–435. [\[CrossRef\]](#)
43. Atkinson, H.V.; Shi, G. Characterization of inclusions in clean steels: A review including the statistics of extremes methods. *Prog. Mater. Sci.* **2003**, *48*, 457–520. [\[CrossRef\]](#)
44. Grabulov, A.; Petrov, R.; Zandbergen, H.W. EBSD investigation of the crack initiation and TEM/FIB analyses of the microstructural changes around the cracks formed under Rolling Contact Fatigue (RCF). *Int. J. Fatigue* **2010**, *32*, 576–583. [\[CrossRef\]](#)

45. Al-Tameemi, H.A.; Long, H. Finite element simulation of subsurface initiated damage from non-metallic inclusions in wind turbine gearbox bearings. *Int. J. Fatigue* **2020**, *131*, 105347. [[CrossRef](#)]
46. Barrow, A.T.W.; Kang, J.H.; Rivera-Díaz-Del-Castillo, P.E.J. The $\rightarrow \eta \rightarrow \theta$ transition in 100Cr6 and its effect on mechanical properties. *Acta Mater.* **2012**, *60*, 2805–2815. [[CrossRef](#)]
47. Lund, T.B. Sub-Surface Initiated Rolling Contact Fatigue—Influence of Non-Metallic Inclusions, Processing History, and Operating Conditions. *J. ASTM Int.* **2010**, *7*, 1–12. [[CrossRef](#)]
48. Vegter, R.; Slycke, J.; Beswick, J.; Dean, S. The Role of Hydrogen on Rolling Contact Fatigue Response of Rolling Element Bearings. *J. Astm Int.* **2010**, *7*, 2. [[CrossRef](#)]
49. Evans, M.H. White structure flaking (WSF) in wind turbine gearbox bearings: Effects of ‘butterflies’ and white etching cracks (WECs). *Mater. Sci. Technol.* **2012**, *28*, 3–22. [[CrossRef](#)]
50. Lewis, M.W.J.; Tomkins, B. A fracture mechanics interpretation of rolling bearing fatigue. *Proc. Inst. Mech. Eng. Part J J. Eng. Tribol.* **2012**, *226*, 389–405. [[CrossRef](#)]
51. Bruce, T.; Long, H.; Dwyer-Joyce, R.S. Threshold Maps for Inclusion-Initiated Micro-Cracks and White Etching Areas in Bearing Steel: The Role of Impact Loading and Surface Sliding. *Tribol. Lett.* **2018**, *66*, 111. [[CrossRef](#)]
52. Grabulov, A. *Fundamentals of Rolling Contact Fatigue*; TU Delft: Delft, The Netherlands, 2010.

Disclaimer/Publisher’s Note: The statements, opinions and data contained in all publications are solely those of the individual author(s) and contributor(s) and not of MDPI and/or the editor(s). MDPI and/or the editor(s) disclaim responsibility for any injury to people or property resulting from any ideas, methods, instructions or products referred to in the content.